Generalized Frequency Scaling and Backprojection for LFM-CW SAR Processing

Evan C. Zaugg, *Member, IEEE*, and David G. Long, *Fellow, IEEE*

Abstract—This paper presents a generalized treatment of image formation for a linear-frequency-modulated continuous wave (LFM-CW) synthetic aperture radar (SAR) signal, which is a key technology in making very small SAR systems viable. The signal model is derived, which includes the continuous platform motion. The effect of this motion on the SAR signal is discussed, and an efficient compensation method is developed. Processing algorithms are developed including precise and approximate backprojection methods and a generalized frequency scaling algorithm that accounts for an arbitrary number of terms of a Taylor expansion approximation of the SAR signal in the Doppler frequency domain. Together, these algorithms allow for the processing of LFM-CW SAR data for a wide variety of system parameters, even in scenarios where traditional algorithms and signal approximations break down.

Index Terms—Radar imaging, synthetic aperture radar (SAR).

I. Introduction

V ERY small synthetic aperture radar (SAR) systems are made possible by using a linear-frequency-modulated continuous wave (LFM-CW) signal that can achieve a good signal-to-noise ratio with lower peak transmit power. Combined with an analog dechirp, these systems can be made with hardware that is simpler and cheaper and consumes less power than traditional SAR systems. This enables the use of low-cost SARs on small unmanned aircraft systems, which opens up a whole range of new applications, permitting SAR imagery to be collected in harsh climates or in environments too dangerous for manned aircraft or expensive SAR systems. The potential of this new technology has been shown in a variety of demonstration systems [1]–[9].

Along with new possibilities come new challenges. The fact that a CW signal is both continuously transmitting and receiving means that processing must take into account the continuous motion of the platform. CW operation requires a separate transmit and receive antenna to separate the signals on the transmit and receive signal paths; also, the direct feedthrough from the transmit to the receive antenna must be controlled.

Several SAR processing algorithms have been adapted for LFM-CW SAR; the literature primarily focuses on the range-Doppler algorithm (RDA) [10], the frequency scaling algorithm (FSA) [11]–[16], and the Omega-K algorithm [17]. For time-domain backprojection, the added complication of dealing with the continuous motion due to the use of a CW signal has only recently been addressed [18], [19]. Moreover, similar to most traditional SAR processing, previously published algorithms make assumptions and approximations (such as a Taylor series expansion in the dechirped-Doppler domain) that lose validity, resulting in phase errors and defocused imagery, when used with extreme SAR parameters.

This paper contains a general treatment of the LFM-CW SAR signal and develops new SAR processing algorithms appropriate for processing CW data, taking care to examine approximations made along the way. We analyze the effects of the continuous platform motion, for linear and nonlinear flight paths, and develop a general correction for the effects. An overview of LFM-CW SAR is provided in Section II with a discussion of the LFM-CW SAR signal. In developing the processing methods, we first discuss high-precision algorithms and then explore the approximations used in developing more computationally efficient algorithms. Section III examines backprojection for LFM-CW SAR and develops an algorithm kernel for handling the continuous motion, both precisely and approximately. In Section IV, we develop a generalized frequency-domain processing method. We first take a look at the RDA and the FSA, showing the signal derivation and the algorithms' dependence on a Taylor expansion, which approximates the signal in the dechirped-Doppler domain (which is similar to the wavenumber domain in traditional pulsed SAR). For certain SAR system parameters, such as low frequencies, large beamwidths, and high squint, neglecting the higher order terms of the Taylor expansion causes defocusing. To address this, an efficient generalized FSA (GFSA) is developed that processes the data using an arbitrary number of terms of the expansion.

II. LFM-CW SAR Signal

An LFM-CW radar continuously transmits a frequency-modulated signal. This signal is a linear-frequency ramp or chirp. In SAR, the radar is carried on a platform, and the radar illuminates the target area. Part of the signal is scattered back to the radar where the receive antenna continuously collects the reflected signal that can then be digitized and processed to form the SAR image.

LFM-CW SAR often uses an analog dechirp to reduce the sample rate required to digitize the signal. A general expression for the dechirped signal, i.e., s_{dc}, is

$$s_{dc}(t,\eta) = e^{\left[j\left(2\pi k_r t(\tau-d) + 2\pi f_0(\tau-d) - \pi k_r(\tau^2-d^2)\right)\right]} \quad (1)$$

where τ is the two-way travel time to a target (which is a function of η), and d is the dechirp delay. The derivation of (1) follows, including a discussion of how τ is approximated for use in SAR processing algorithms.

A. Derivation of the Dechirped Signal

The frequency of the LFM-CW signal increases from a starting frequency f_0 and spans the bandwidth BW, at the chirp rate $k_r = BW \cdot PRF$. This cycle is repeated at the PRF, giving a PRI equal to the pulse length, i.e., T_p. The transmitted up-chirp signal can be expressed in the time domain, where t is fast time, and η is slow time, as

$$s_t(t,\eta) = \exp\left[j(\phi + 2\pi f_0 t + \pi k_r t^2)\right] \quad (2)$$

where ϕ is the initial phase. A down-chirp signal is similar, with $f_{0d} = f_0 + BW$ being the starting frequency and $-k_r$ being the chirp rate.

At time t, the radar is also receiving the reflected signal transmitted at time $t - \tau$, where τ is the two-way time-of-flight to a target. τ is calculated using the range-to-target, which is different from time t and time $t - \tau$ due to the constant motion of the aircraft. With τ constantly changing, it can be unclear what value of τ should be used in the processing algorithms. The traditional SAR algorithms, using the stop-and-go approximation, use a signal model where the platform is stationary for transmitting and receiving each pulse. This way, τ is a function of the slow-time variable η, which has discrete values for the slow time of each radar pulse. In reality, the platform moves during the pulse, and the range-to-target changes during the pulse. This continuous motion can be modeled by allowing τ to vary in fast time, as a function of t, as well as the discrete slow-time steps in η. The constant motion also means that the signal travels a different distance to and from the target; however, for most airborne applications, this difference can be neglected while still modeling the change in range over the length of the pulse. Unless the platform velocity and range-to-target are very large, the expression for τ can be simplified to $\tau \approx 2R(t,\eta)/c_0$, where $R(t,\eta) = \sqrt{R_0^2 + v^2(t+\eta)^2}$, and R_0 is the range of closest approach to the target. This gives us an expression for τ that includes the continuous motion of the platform and, thus, a continuous change in range-to-target. A method of making the precise calculation for τ is shown in Appendix A.

Going forward with the approximation $\tau \approx 2R(t,\eta)/c_0$, the received signal from a target at range $R(t,\eta)$, with time delay τ is

$$s_r(t,\eta) \approx \exp\left[j\left(\phi + 2\pi f_0(t-\tau) + \pi k_r(t-\tau)^2\right)\right]. \quad (3)$$

The transmit signal is mixed with the received signal and low-pass filtered in hardware, which is mathematically equivalent to multiplying (2) by the complex conjugate of (3). This results in the dechirped signal s_{dc0}

$$s_{dc0}(t,\eta) = \exp\left[j(2\pi f_0\tau + 2\pi k_r t\tau - \pi k_r\tau^2)\right]. \quad (4)$$

This is the signal for LFM-CW SAR systems with a direct dechirp [1], [2], [5], [9]. The available swath width is often limited when using a direct dechirp because a large portion of the sampling bandwidth is used to record data that correspond to the empty space between the SAR and the ground. A system with a delayed dechirp [25] can ignore data from ranges nearer than a minimum range determined by the duration of the delay. By doing this, the radar more efficiently utilizes the radar's resources, providing a wider ground swath.

Alternatively, the return signal is mixed with a copy of the transmit signal delayed by d

$$s_{td}(t,\eta) = \exp\left[j\left(\phi + 2\pi f_0(t - d) + \pi k_r(t - d)^2\right)\right]. \quad (5)$$

The dechirped signal can then be expressed by multiplying (5) by the complex conjugate of (3), resulting in (1).

In the dechirped signal, each frequency directly correlates to a given range, i.e., $f_r = 2Rk_r/c_0$. The sampling rate of an LFM-CW SAR can be much less than a traditional SAR by limiting the range. For a direct dechirp (no delay, $d = 0$), the sampling bandwidth directly corresponds to the maximum range that can be imaged, i.e.,

$$f_s = \frac{2R_{\max}k_r}{c_0}. \quad (6)$$

For a delayed dechirp, this maximum range is shifted by the delay, i.e.,

$$f_s = \frac{2R_{\max}k_r}{c_0} - d \cdot k_r = \frac{2R_{\max}k_r}{c_0} - \frac{2R_{\min}k_r}{c_0}. \quad (7)$$

A small LFM-CW SAR may be limited to a small sampling bandwidth due to hardware constraints driven by the need to reduce the size, weight, and power consumption. This can severely limit the imaging swath width. A delayed dechirp shifts more ranges into the sampling bandwidth, allowing for a wider swath. The delay is set to the nearest range desired in the image—the frequencies increase with range from that point. This way, none of the sampling bandwidth is wasted on any range nearer the platform than this minimum range.

To remove returns from targets outside the desired swath, LFM-CW SAR systems usually employ a bandpass filter with high out-of-band rejection [5], [9], [25]. For targets at ranges farther than the maximum range with a corresponding frequency higher than the sampling rate, aliasing can occur, placing the target return within the swath. It is important that the bandpass filter attenuates such signals to avoid ambiguities. For a delayed dechirp, there can be targets nearer the radar than the minimum range. The frequencies from such targets can fold over into the sampling band when the signal is dechirped to baseband. One solution is to dechirp the signal to an intermediate frequency, apply the bandpass filter, then mix to baseband [25] to avoid near-range ambiguities.

B. Derivation of the Range-Compressed Signal

Range compression of the dechirped signal consists of a Fourier transform in fast time. Calculating an expression for the range-compressed signal is simplified by assuming no motion during the chirp. This incorrect assumption is a good starting point for deriving a more accurate expression. It is equivalent to assuming that R is not a function of t. With $\tau = 2R/c_0$, the range Fourier transform of (1) is calculated with the integral, i.e.,

$$
\begin{aligned}
S_R &= \int_{\frac{2R}{c_0}}^{\frac{2R}{c_0}+T_p} s_{dc}(t,\eta) \exp[-j2\pi f_r t] \, dt \\
&\approx \frac{\frac{1}{2}j\left(-e^{[j\pi T_p(f_r+k_r d-k_r\tau)]} + e^{[-j\pi T_p(f_r+k_r d-k_r\tau)]}\right)}{\pi(f_r+k_r d-k_r\tau)} \\
&\quad \cdot \frac{\exp[j\pi\Phi_{rc}]}{\pi(f_r+k_r d-k_r\tau)} \\
&\approx T_p \operatorname{sinc}[T_p(f_r+k_r d-k_r\tau)]\exp[j\pi\Phi_{rc}] \qquad (8)
\end{aligned}
$$

where

$$
\Phi_{rc} = k_r T_p(\tau-d) - f_r T_p + \frac{4k_r R(\tau-d)}{c_0}
$$

$$
+ 2f_0(\tau-d) - k_r(\tau^2-d^2) - \frac{4f_r R}{c_0}. \qquad (9)
$$

When there is no dechirp delay, i.e., $d = 0$, this simplifies to

$$
\begin{aligned}
S &\approx T_p \operatorname{sinc}\left[T_p\left(f_r - \frac{2k_r R}{c_0}\right)\right] \\
&\quad \cdot \exp\left[j\pi\left(\frac{2k_r R T_p}{c_0} - f_r T_p + \frac{4k_r R^2}{c_0^2} + \frac{4f_0 R}{c_0} - \frac{4f_r R}{c_0}\right)\right].
\end{aligned} \qquad (10)
$$

In order to explore what happens when we include the motion during the chirp, we assume a linear platform motion model, calculate the two-way time-of-flight to a target, and approximate the change in range as linear during a single chirp; thus

$$
\begin{aligned}
\tau(t,\eta) &= \frac{2\sqrt{R_0^2 + v^2(\eta+t)^2}}{c_0} \\
&\approx \frac{2R(0,\eta)}{c_0} + \frac{2v^2\eta t}{R(0,\eta)c_0}
\end{aligned} \qquad (11)
$$

where $R(0,\eta) = \sqrt{R_0^2 + v^2\eta^2}$, and R_0 is the range of closest approach.

Substituting the approximation in (11) for τ in (1) and (4) and rearranging the terms yield

$$
s_{dcm}(t,\eta) = s_{dc}(t,\eta) \exp[j\Phi_m] \qquad (12)
$$
$$
s_{dcm0}(t,\eta) = s_{dc0}(t,\eta) \exp[j\Phi_m] \qquad (13)
$$

where

$$
\Phi_m = \left(-\frac{4v^4\eta^2\pi k_r}{R^2 c_0^2} + \frac{4v^2\eta\pi k_r}{R c_0}\right)t^2
$$

$$
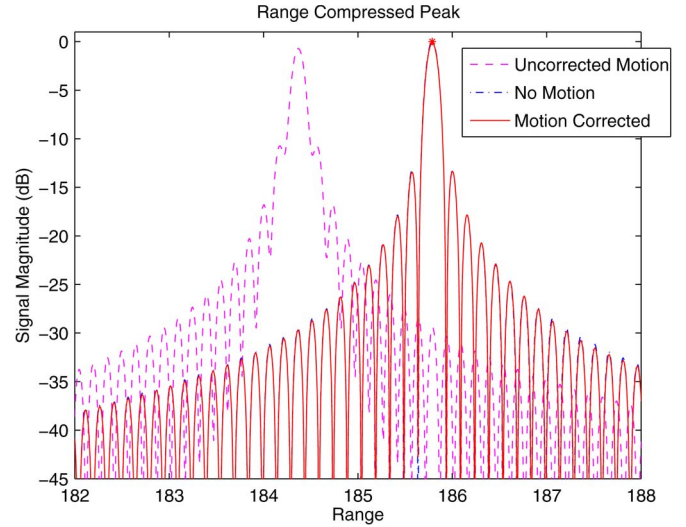+ \left(\frac{-8v^2\eta\pi k_r}{c_0^2} + \frac{4v^2\eta\pi f_0}{R c_0}\right)t. \qquad (14)
$$

Fig. 1. SAR data of a single point target are simulated and range compressed. This figure shows cuts of this range-compressed data at the edge of the azimuth beam, i.e., on the far-left edge in Fig. 2. The asterisk shows where the target peak should be, which is the range to the target at the time of the chirp shown in the figures. The effects of the continuous motion are clearly seen in the magenta line, where the peak is shifted and is wider. The results from having no motion during the chirp and from applying a correction to the continuous-motion-shifted data are nearly identical (the blue and the red lines lay almost entirely on top of one another).

The effects of continuous motion on the signal phase can be seen by inspecting (14). As the range-to-target changes during a chirp, a change in frequency is introduced. The t^2 terms represent this chirp caused by the platform motion. The Fourier transform of this chirp is rect-like, and when convolved with (8) results in a spreading of the impulse response, as demonstrated in Fig. 1.

The motion also induces an effect on the carrier frequency, visible in the t terms. Additional insight can be gained by noticing that the final term is the Doppler frequency. Using the geometry in Fig. 3, the Doppler frequency is

$$
2\pi f_d = 2\pi \frac{2v\sin(\theta_s)}{\lambda} = 2\pi 2v\frac{v\eta}{R}\frac{f_0}{c_0}. \qquad (15)
$$

By inspection, the second t term in (14) is much larger than all the other terms and is the dominant effect of the platform motion: a frequency shift equal to the Doppler frequency, which translates into a range shift in the range-compressed data, as is visible in Figs. 1 and 2. The terms with c_0^2 in the denominator are orders of magnitude smaller than the other terms, and for any airborne or orbital SAR, t will be much less than 1, making the t^2 terms smaller than the t terms.

If we neglect the small terms and rewrite (14) in terms of f_d, we obtain a convenient range-independent expression that can correct for the effects of continuous motion. This simplified term is equivalent to the continuous-motion term derived in the signal model presented in [12]. The phase of this approximate correction is

$$
\Phi_{cor} = -2\pi f_d t. \qquad (16)
$$

Because the correction is expressed in terms of Doppler frequency, which is a measure of the continuous change in range
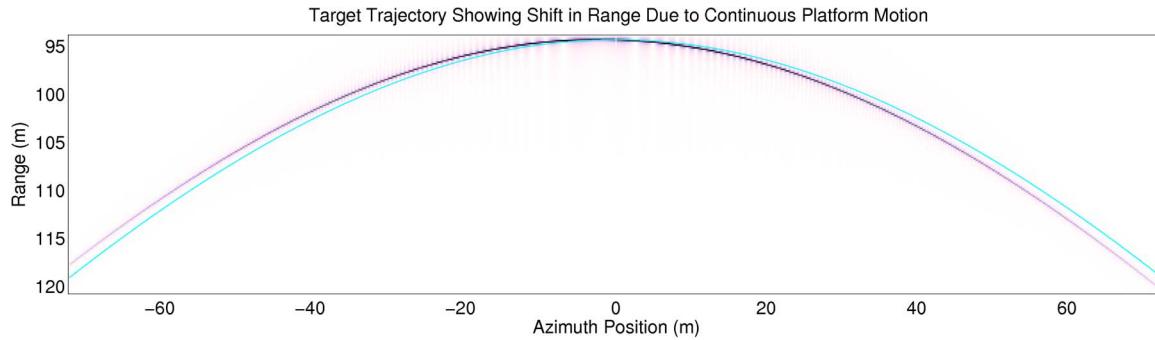
Fig. 2. Range-compressed simulated SAR data for a single point target showing the range shift due to the continuous platform motion. The narrow solid line (the bottom line on the left side of the image and the top line on the right) represents the actual range-to-target for each azimuth position. The other line is the range-compressed SAR data, which are clearly shifted in range due to the platform motion.
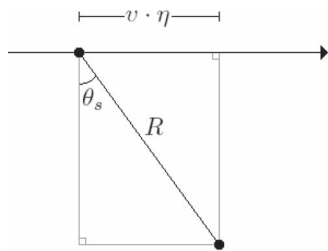

Fig. 3. SAR imaging geometry, the SAR flies to the right following the arrow. A target at range R is at a squint angle of θ_s. The Doppler frequency of the signal return can be calculated from the angle or the distance to the point of closest approach (calculated as velocity times time, $v \cdot \eta$), according to (15).

to the target, the shift caused by the continuous motion of flight can be corrected. The correction also shows good results when applied to data collected with an arbitrary platform path, as demonstrated in Fig. 5.

The change in range needs to be precisely known to properly form a well-focused SAR image. The traditional SAR imaging scenario involves the platform moving in a straight line (or nearly a straight line with motion corrections [13]) where the change in range can be expressed as a hyperbolic function. Many processing algorithms are built around the assumption of a linear flight path. However, the increasing popularity of backprojection methods has made processing SAR data collected from nonlinear flight paths gain more attention in recent studies [23]. In any case, traditional SAR processing algorithms assume that the platform is stationary during a pulse; however, with the continuous transmit and receive of LFM-CW SAR, the continuous motion of the platform causes noticeable degradation in image quality if not properly accounted for. In the following sections, we develop processing algorithms that account for the continuous platform motion, starting with a general backprojection algorithm that handles arbitrary flight paths.

III. LFM-CW BACKPROJECTION

Backprojection normally operates on interpolated range-compressed data. For dechirped SAR, the range-compressed signal can be formed from (8) and (12) in Section II-B. The range-compressed signal can be expressed as a function of range frequency. Range frequency has a direct relationship to

the distance to the target (the target range) according to $f_r = 2Rk_r/c_0$. Thus

$$S_R(f_r, \eta) \approx \mathcal{F}_t \left\{ e^{[j\Phi_m]} \right\} * T_p \operatorname{sinc} \left[T_p \left(f_r - \frac{2k_r R}{c_0} \right) \right]$$

$$\cdot e^{\left[j \left(\frac{4\pi f_0 R}{c_0} - \pi T_p f_r + \frac{2\pi T_p k_r R}{c_0} - \frac{4\pi f_r R}{c_0} + \frac{4\pi k_r R^2}{c_0^2} \right) \right]} \quad (17)$$

where $\mathcal{F}_t$ is a Fourier transform in range, $*$ is convolution, and $\exp[j\Phi_m]$ represents the effects of the continuous platform motion expressed in (14). In this case, the interpolation and range compression can be performed by means of zero padding and a range Fourier transform. However, the continuous platform motion does complicate the issue. If the continuous motion is not taken into account, then the range shift and widened width of the range-compressed target response can cause defocusing in the backprojected image.

It is instructive to start the analysis by examining backprojection without the continuous motion. The signal is digitized in discrete pulses, each pulse number, m, corresponding to a certain value of η. This digitized signal is interpolated to provide an indexed value for each range required for the processing. This indexed range, i.e., $r[m]$, is the distance from a given location in the backprojected image grid to the platform antenna phase center for chirp number m. The range-compressed signal interpolated to range $r[m]$ can then be expressed, with $f_r = 2r[m]k_r/c_0$, as

$$S_{Rm}(r[m]) \approx T_p \operatorname{sinc} \left[T_p \left(f_r - \frac{2k_r r[m]}{c_0} \right) \right]$$

$$\cdot e^{\left[j \left(\frac{4\pi f_0 r[m]}{c_0} - \pi T_p f_r + \frac{2\pi T_p k_r r[m]}{c_0} - \frac{4\pi f_r r[m]}{c_0} + \frac{4\pi k_r r[m]^2}{c_0^2} \right) \right]}. \quad (18)$$

Then, for a pixel located at (x_0, y_0, z_0), the traditional SAR backprojection algorithm can be expressed as

$$A(x_0, y_0, z_0) = \sum_m S_{Rm}(r[m]) \exp\left[j\Phi_e(r[m]) \right] \quad (19)$$

where $A(x_0, y_0, z_0)$ is the complex pixel value, $r[m]$ is the distance to that pixel location, and $\Phi_e(r[m])$ is the complex conjugate of the expected phase for range $r[m]$. $\Phi_e(r[m])$ is
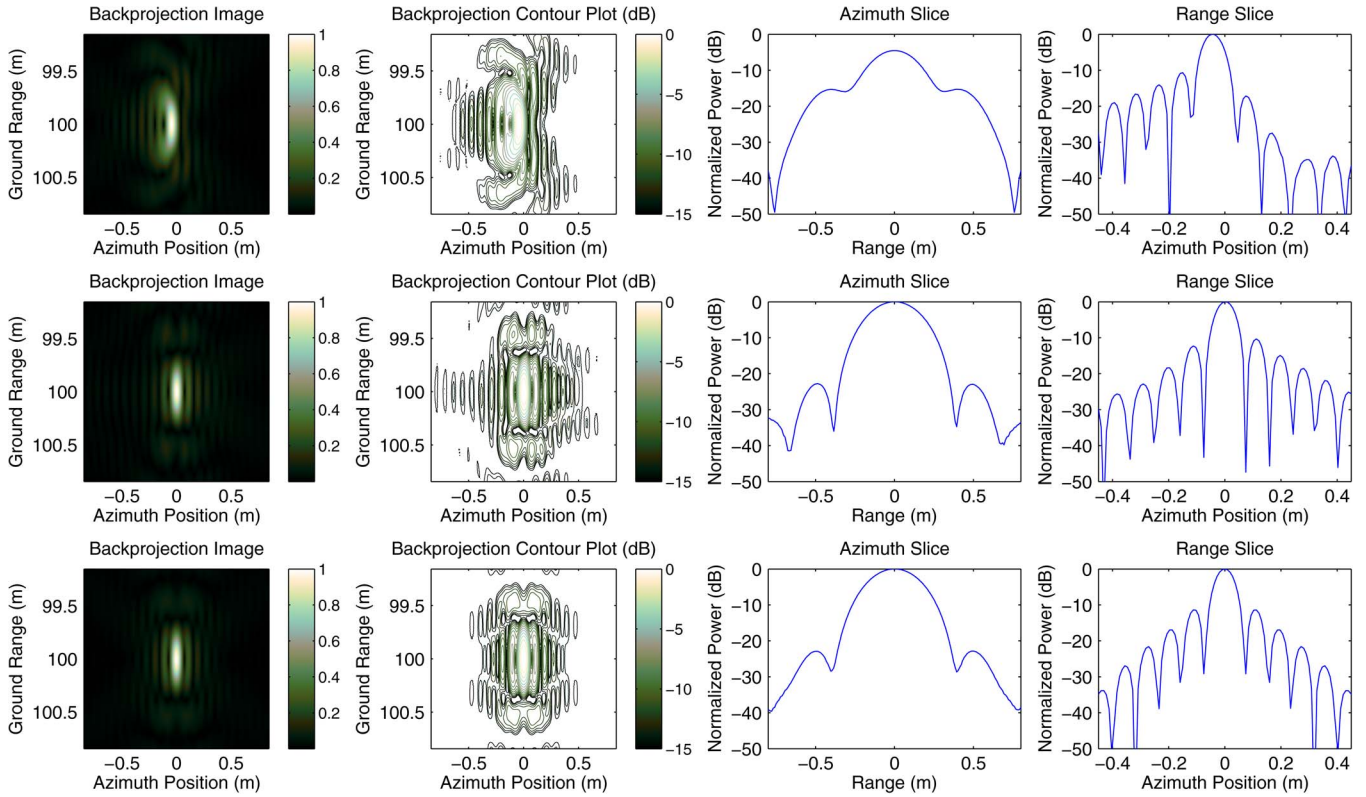
Fig. 4. Simulated SAR data for a point target with a linear trajectory, a bandwidth from 1.5 to 2 GHz, and a 65° beamwidth with no squint, processed with the backprojection algorithm in Section III. The leftmost column shows the magnitude of the focused SAR image, the second column shows a contour plot of the focused image, and the two columns on the right show an azimuth slice and a range slice, respectively, through the center of the target. The first row shows defocusing and a shift in the target location due to the uncompensated continuous platform motion. In the second row, the continuous motion is efficiently compensated using the correction of (16), and in the third row, the continuous motion is inefficiently accounted for using the exact backprojection of (21).

found by taking (9), allowing $f_r = 2r[m]k_r/c_0 - k_r d$, simplifying and conjugating to obtain

$$\Phi_e\left(r[m]\right) = \frac{4\pi k_r r[m]^2}{c_0^2} - \frac{4\pi f_0 r[m]}{c_0} - \pi k_r d^2 + 2\pi f_0 d. \quad (20)$$

The advantages of backprojection include the simplicity of the algorithm, the parallel computation structure, the ability to process data from an arbitrary platform path, and the ability to project the data onto a 3-D grid. A disadvantage is that the algorithm is very computationally taxing, although exploiting the parallel nature of the algorithm and the parallel processing capabilities of modern general-purpose graphic processor units can greatly improve the processing time. (The authors have reported a $300\times$ speedup in backprojection processing between using the main CPU on a standard PC with backprojection programmed in C and using an NVIDIA C1060 Tesla card [24] on the same PC.) The motion of the platform must be precisely known in order to get good results from backprojection. These advantages and disadvantages, as well as the relevant operational considerations for backprojection, are well known to the SAR processing community.

In using backprojection to process LFM-CW SAR data, it is important to account for the spreading and shifting effects visible in the range-compressed data due to the continuous platform motion [19]. There are several of ways to do this. The first is to use the raw data directly, without range compression

(referred to as time-domain correlation in [18]). This method is of very limited practical relevance and is included here for completeness. The platform position for each *sample* of raw data is used. In this case, the backprojection operation expands to

$$A_2(x_0, y_0, z_0) = \sum_{t_i} \sum_m s_{dc}[t_i, m] \exp\left[j\left(\Phi_{e2}[t_i, m]\right)\right] \quad (21)$$

where Φ_{e2} is the conjugate of the phase in (1) or (4), and the $\tau[t_i, m]$ buried inside s_{dc} and Φ_{e2} is the continuously changing two-way time of flight to the point (x_0, y_0, z_0) at the discrete fast-time sample t_i and pulse number m. This is a very exact method, but is even more computationally taxing than the conventional backprojection algorithm, and it is unlikely that it would ever be practically used.

The second (and more efficient) option for accounting for the continuous motion is to use the correction presented in (16) to correct for the effects of the continuous motion and then apply the standard backprojection in (19). Similar results are obtained in [18] where a modified backprojection algorithm is defined, which uses a continuous-motion component in the expression for the range between radar and target pixel. In Fig. 4, simulated SAR data with a standard linear trajectory is processed with and without accounting for the continuous platform motion showing the effects on the image quality. In Fig. 5, the platform trajectory is circular, showing how the same continuous motion corrections also work for nonlinear flight paths.
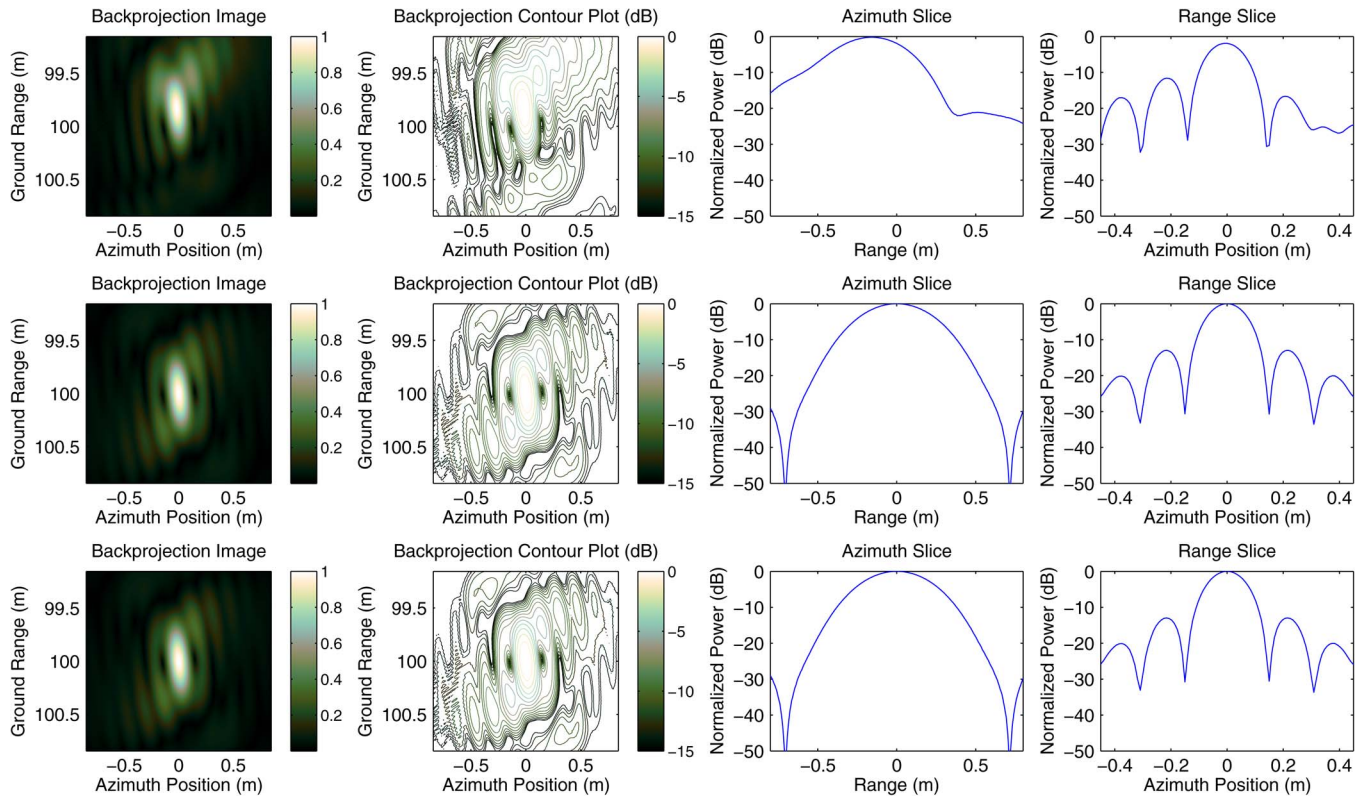
Fig. 5. Simulated SAR data from a quarter of a circular path, where the target is located near the far edge of the circle, with the same SAR parameters and image layout as in Fig. 4. The first row neglects continuous motion, the middle row corrects for the motion using (16), and the bottom row is from exact processing in (21). The description of the columns is the same as in Fig. 4.

IV. GENERALIZED FREQUENCY-DOMAIN PROCESSING

Frequency-domain methods have been developed, such as the RDA [10] and the FSA [11], which make approximations that allow for faster processing but result in reduced accuracy in situations where the approximations lose validity. These algorithms apply a series of matched filters and scaling terms or interpolations to compress the data in range and azimuth and remove the range cell migration. Both of these algorithms depend upon a Taylor series approximation of the signal in the dechirped-Doppler domain. Low orders of this approximation are only valid for a limited set of SAR parameters, which prevent these algorithms from properly focusing the SAR data when the radar parameters push beyond the validity of the approximation.

This section derives an expression for the SAR signal in the dechirped-Doppler domain. The Taylor expansion of the signal and the errors it introduces are then discussed. The relationship between the Taylor approximation and the frequency-domain processing algorithms is shown. To overcome the limits of these algorithms, a GFSA that includes an arbitrary number of terms of the expansion is developed.

A. Derivation of LFM-CW SAR Signal in the Dechirped-Doppler Domain

In processing, an azimuth Fourier transform of the raw dechirped data puts the data in the dechirped-Doppler domain. Analytically computing the azimuth Fourier transform for (1) is

impractical; hence, finding an expression for the signal requires some algebraic manipulation and an approximation. Using a method outlined in [20] and [21], we start with the range-compressed data and make an approximation of the original dechirped signal. This approximation allows the azimuth Fourier transform to be analytically tractable. Starting with (17), we, for convenience, rewrite the last five exponential terms as $\exp j[A_s + B_s + C_s + D_s + E_s]$.

As in [20] and [21], the inverse Fourier transform is facilitated by making a substitution and multiplying (17) by 1, or

$$e^{\left[\left(-j\frac{\pi}{k_r}f_r^2\right)\right]} e^{\left[j\left(\frac{\pi}{k_r}f_r^2\right)\right]} = e^{\left[j\left(-\frac{\pi}{k_r}f_r^2 + G_s\right)\right]}. \quad (22)$$

The substitution is

$$F = f_r - \frac{2k_r R}{c_0} \quad (23)$$

and we note that

$$-\pi T_p F = -\pi T_p f_r + \frac{2\pi T_p k_r R}{c_0} = B_s + C_s \quad (24)$$

$$\frac{\pi}{k_r} F^2 = \frac{\pi}{k_r} f_r^2 - \frac{4\pi f_r R}{c_0} + \frac{4\pi k_r R^2}{c_0^2} = G_s + D_s + E_s. \quad (25)$$

We can now rewrite (17) as

$$S_R = \mathcal{F}_t\left\{e^{[j\Phi_m]}\right\} * T_p \operatorname{sinc}[T_p F] \cdot e^{\left[j\frac{4\pi f_0 R}{c_0}\right]}$$
$$\cdot e^{\left[-j\pi T_p F\right]} e^{\left[j\frac{\pi}{k_r}F^2\right]} e^{\left[-j\frac{\pi}{k_r}f_r^2\right]}. \quad (26)$$

The inverse Fourier integral is also expressed applying the F substitution, i.e.,

$$
\int_{-\infty}^{\infty} \exp[j2\pi f_r t]df_r = \int_{-\infty}^{\infty} \exp\left[j2\pi\left(F + \frac{2k_r R}{c_0}\right)t\right]dF
$$

$$
= \exp\left[j\frac{4\pi k_r Rt}{c_0}\right]\int_{-\infty}^{\infty} \exp[j2\pi Ft]dF
$$

(27)

and the inverse Fourier integral for (26) is computed, i.e.,

$$
s_{dc0} \approx e^{[j\pi k_r t^2]}
$$

$$
* \left\{ e^{[j\Phi_m]}T_p e^{\left[j\frac{4\pi f_0 R}{c_0}\right]} e^{\left[j\frac{4\pi k_r Rt}{c_0}\right]} \right.
$$

$$
\left. \cdot \int_{-\infty}^{\infty} \text{sinc}[T_p F]\, e^{[-j\pi T_p F]}\, e^{\left[j\frac{\pi}{k_r}F^2\right]}\, e^{[j2\pi Ft]}dF \right\}
$$

$$
\approx e^{[j\pi k_r t^2]} * \left\{ \text{rect}\left(\frac{t-T_p}{T_p}\right) e^{\left[j\Phi_m + j\frac{4\pi f_0 R}{c_0} + j\frac{4\pi k_r Rt}{c_0}\right]} \right\}
$$

(28)

where the F^2 term is neglected in computing the integral. Neglecting the F^2 term is a good approximation for a large time-bandwidth product [20], [21], and allows for computing the azimuth Fourier transform of the approximated dechirped signal. The sinc function transforms into a rect function shifted by the F terms. The term on the left-hand side of the convolution in the last line of (28) is known as the residual video phase (RVP) term [20], [21].

The azimuth Fourier transform for the signal can be computed using the principle of stationary phase. We express the phase of the signal within the curly brackets on the bottom line of (28) using the same approximation for the continuous motion as in the motion correction developed in (16). This phase is

$$
\phi_s = 2\pi f_d t + \frac{4\pi f_0 R}{c_0} + \frac{4\pi k_r Rt}{c_0}.
$$

(29)

We use the linear-flight-path assumption, substituting $R = \sqrt{R_0^2 + v^2\eta^2}$ into (29) and setting the derivative of $\phi_s - 2\pi f_a \eta$ with respect to η equal to zero, where f_a is the azimuth frequency variable, resulting in

$$
\frac{4\pi f_0 v^2 \eta}{c_0 \sqrt{R_0^2 + v^2\eta^2}} + \frac{4\pi k_r t v^2 \eta}{c_0 \sqrt{R_0^2 + v^2\eta^2}} - 2\pi f_a = 0.
$$

(30)

The stationary point is found by solving for η

$$
\eta = \frac{c_0 f_a R_0}{v\sqrt{-f_a^2 c_0^2 + 4v^2 f_0^2 + 8v^2 f_0 k_r t + 4v^2 k_r^2 t^2}}.
$$

(31)

Then, the phase of the signal after the azimuth Fourier transform, i.e., Φ_{S_A}, is found by substituting (31) back into $\phi_s - 2\pi f_a \eta$. With some algebraic manipulation, the expression for

the phase of the signal in the dechirped-Doppler domain, i.e., Φ_{S_A}, simplifies to

$$
\Phi_{S_A} \approx \left(\frac{-\pi k_r f_d^2}{f_0^2} + \frac{2\pi k_r f_d}{f_0}\right)t^2 + 2\pi f_d t
$$

$$
+ \frac{4\pi(f_0 + k_r t)\sqrt{R_0^2 + \frac{c_0^2 f_a^2 R_0^2}{-f_a^2 c_0^2 + 4v^2 f_0^2 + 8v^2 f_0 k_r t + 4v^2 k_r^2 t^2}}}{c_0}
$$

$$
- \frac{2\pi f_a^2 c_0 R_0}{v\sqrt{-f_a^2 c_0^2 + 4v^2 f_0^2 + 8_v^2 f_0 Krt + 4v^2 k_r^2 t^2}}
$$

$$
\approx \left(\frac{-\pi k_r f_d^2}{f_0^2} + \frac{2\pi k_r f_d}{f_0}\right)t^2 + 2\pi f_d t
$$

$$
+ \frac{\frac{8\pi(f_0 + k_r t)^2 v R_0}{c_0} - \frac{2\pi f_a c_0 R_0}{v}}{\sqrt{-f_a^2 c_0^2 + 4v^2 f_0^2 + 8v^2 f_0 k_r t + 4v^2 k_r^2 t^2}}
$$

$$
\approx \left(\frac{-\pi k_r f_d^2}{f_0^2} + \frac{2\pi k_r f_d}{f_0}\right)t^2 + 2\pi f_d t
$$

$$
+ \frac{4\pi R_0}{\lambda}\sqrt{\left(1 + \frac{k_r \lambda t}{c_0}\right)^2 - \frac{f_a^2 \lambda^2}{4v^2}}.
$$

(32)

The Doppler frequency is an equivalent way to express the azimuth frequency, thus $f_d = f_a$, the exponentials that make up the signal in the dechirped-Doppler domain can be expressed in

$$
S_A = \exp[j\pi k_r t^2]
$$

$$
* e^{\left[j\left[\left(\frac{-\pi k_r f_a^2}{f_0^2} + \frac{2\pi k_r f_a}{f_0}\right)t^2 + 2\pi f_a t\right]\right]}
$$

$$
\times e^{\left[j\left[\frac{4\pi R_0}{\lambda}\sqrt{\left(1 + \frac{k_r \lambda t}{c_0}\right)^2 - \frac{f_a^2 \lambda^2}{4v^2}}\right]\right]}
$$

(33)

which is a very good approximation of the signal, as illustrated in Fig. 6(a), which reveals only a small variation in the phase difference, roughly linear in azimuth frequency, between the actual phase and this approximation over the support band, indicating a small error due to the approximation. This error is due to neglecting the F^2 term in (28).

The effects of the continuous platform motion can be removed at this point by multiplying (33) by (16). Once that is done, algorithms based on a Taylor series expansion of the dechirp-Doppler domain signal can be derived.

B. Taylor Expansion of the SAR Signal

Typical processing algorithms use a Taylor series approximation of the square root term in (33) about the point $t = 0$. To simplify the analysis, we define a range curvature term, i.e.,

$$
D(f_\eta) = \sqrt{1 - \frac{f_a^2 \lambda^2}{4v^2}}
$$

(34)

then substitute it into the square root term in (33) and expand, i.e.,

$$
\Upsilon(t) = \sqrt{\left(1 + \frac{k_r \lambda t}{c_0}\right)^2 - 1 + D^2(f_\eta)}
$$

$$
\approx \Upsilon(0) + \frac{\Upsilon'(0)}{1!}t + \frac{\Upsilon''(0)}{2!}t^2 + \frac{\Upsilon'''(0)}{3!}t^3 \cdots
$$

$$
\approx Y_0 + Y_1 t + \frac{Y_2}{2!}t^2 + \frac{Y_3}{3!}t^3 \cdots
$$

(35)

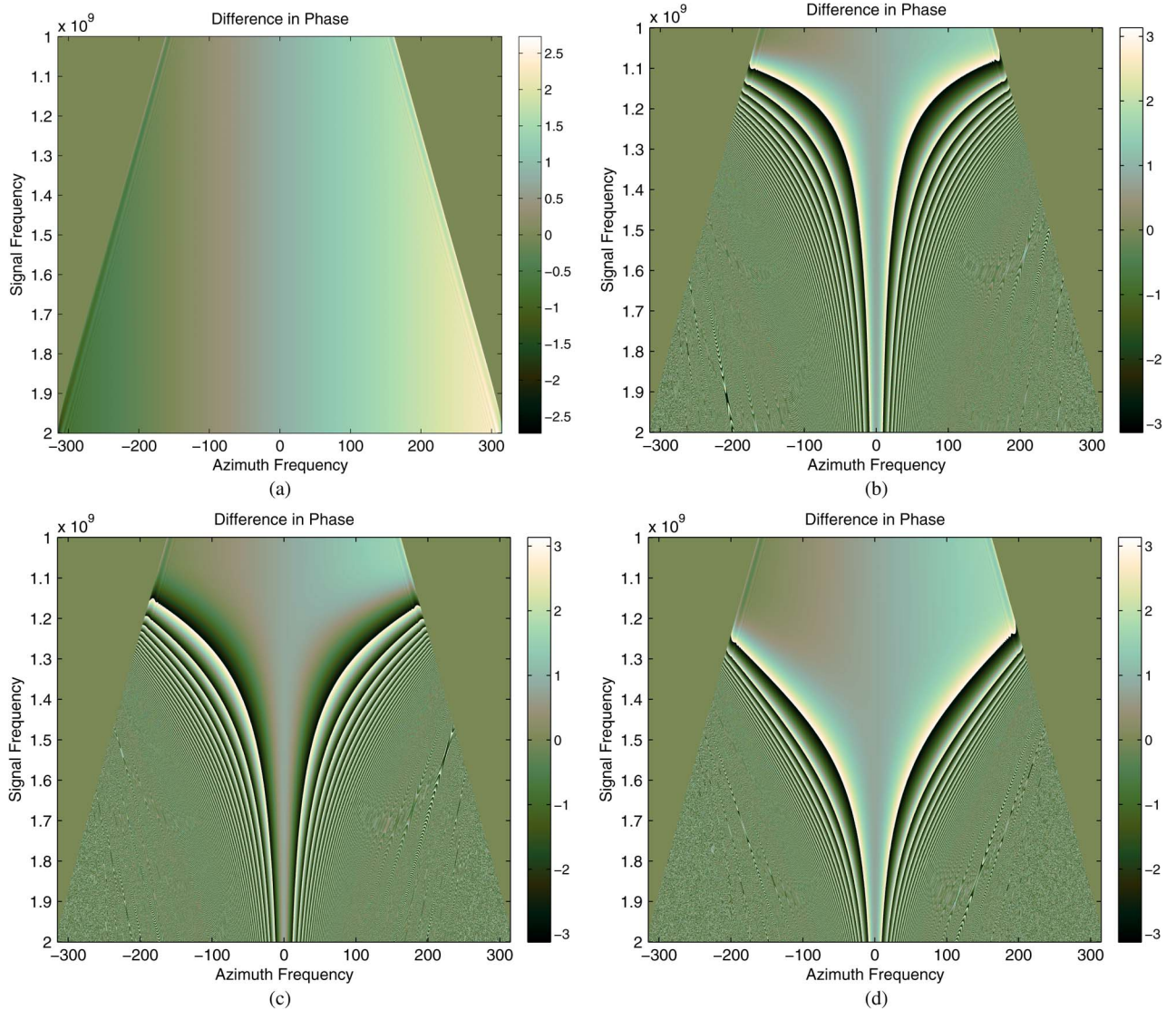where Y_i is the ith derivative of $\Upsilon(t)$ evaluated at $t = 0$.

Fig. 6. These figures show the phase difference between the azimuth Fourier transform of simulated SAR data for a single point target and analytical approximations for the signal from (33) and (37). Ideally, the phase difference would be constant over the bandwidth, which results in good focusing, whereas a rapidly varying phase difference indicates a poor match for the signal, resulting in defocused imagery. The simulated data shown have a bandwidth from 1 to 2 GHz, a beamwidth of 57°, and a velocity of 50 m/s. The transmit signal frequency slowly chirps over the bandwidth during the entire sampling interval repeating each pulse. The support band has a trapezoidal shape because the Doppler bandwidth is smaller for a fixed beamwidth at lower frequencies. Ideally, the phase difference is constant over the support band; however, each approximation falls short of this ideal. (a) With the approximation from (33), there is little variation in the phase difference over the support band. This indicates that the approximation is very close to the actual signal phase. When used in an image formation algorithm, the whole support band constructively contributes in generating a well-focused image, as seen in Fig. 8. (b) A second-order approximation from (37) has a very small portion of the support band (the upper and middle sections) that has a nearly constant phase difference. When used in an image formation algorithm, only a small portion of the support band contributes to properly focusing the target, which results in a poorly focused image, as seen in Fig. 8. (c) A third-order approximation has a larger portion of the support band that is useful for image formation. (d) A sixth-order approximation results in better focusing.

The phase error of this approximation can be expressed as

$$\phi_{Error} = \frac{4\pi R_0 \left[\Upsilon(t) - \sqrt{\frac{k_r \lambda t (2c_0 + k_r \lambda t)}{c_0^2} + D^2(f_\eta)} \right]}{\lambda} \quad (36)$$

which is a function of the following four parameters:

1) the range-to-target, R_0;
2) the center frequency, f_0;
3) the chirp rate times fast time, $k_r t$;
4) the azimuth frequency, f_η.

The phase error gets larger as the range increases, the center frequency decreases, the product of the chirp rate times t increases, and/or the azimuth frequency increases. The product of the chirp rate times fast time grows with increases in bandwidth, whereas the azimuth frequency increases with wider antenna beamwidths.

In Fig. 6(b), we see that for a second-order approximation of the signal [as in (35)], only a small portion of the frequency support band is usable due to the large phase errors [as calculated in (36)]. As suggested in Fig. 6(c) and (d), including more high-order terms in the approximation reduces the phase error, making more of the support band usable. Other small phase
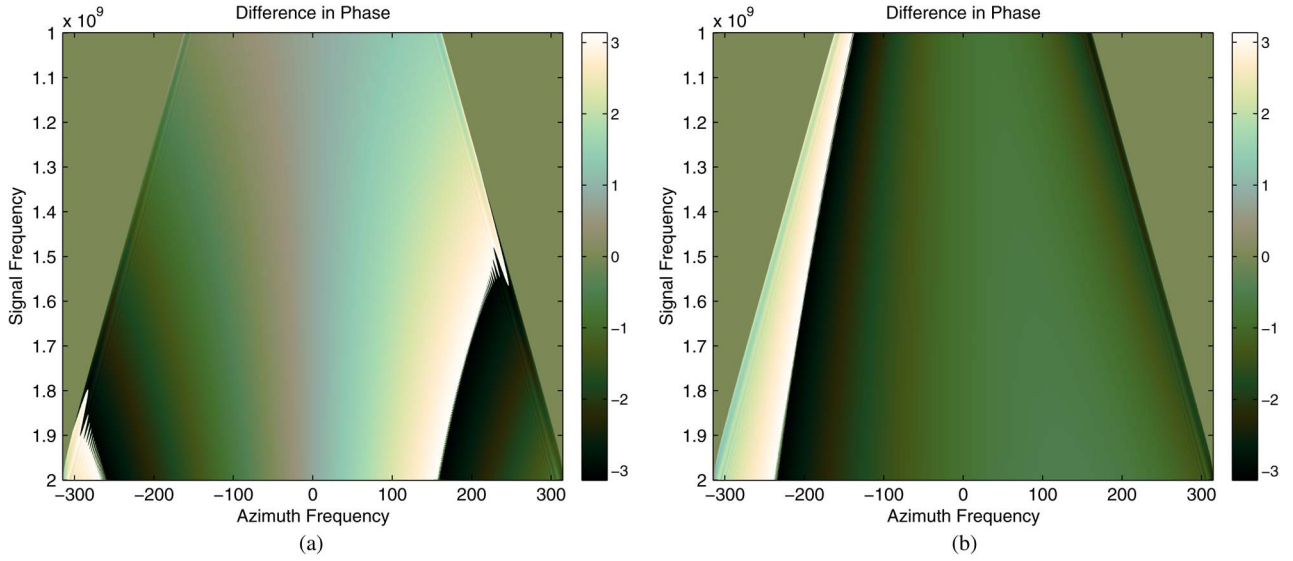
Fig. 7. These figures show the phase difference, as in Fig. 6(a). (a) Neglecting the continuous-platform-motion term in the approximation from (33) increases the phase error. (b) Neglecting the RVP correction with the approximation from (33) also increases the phase error.
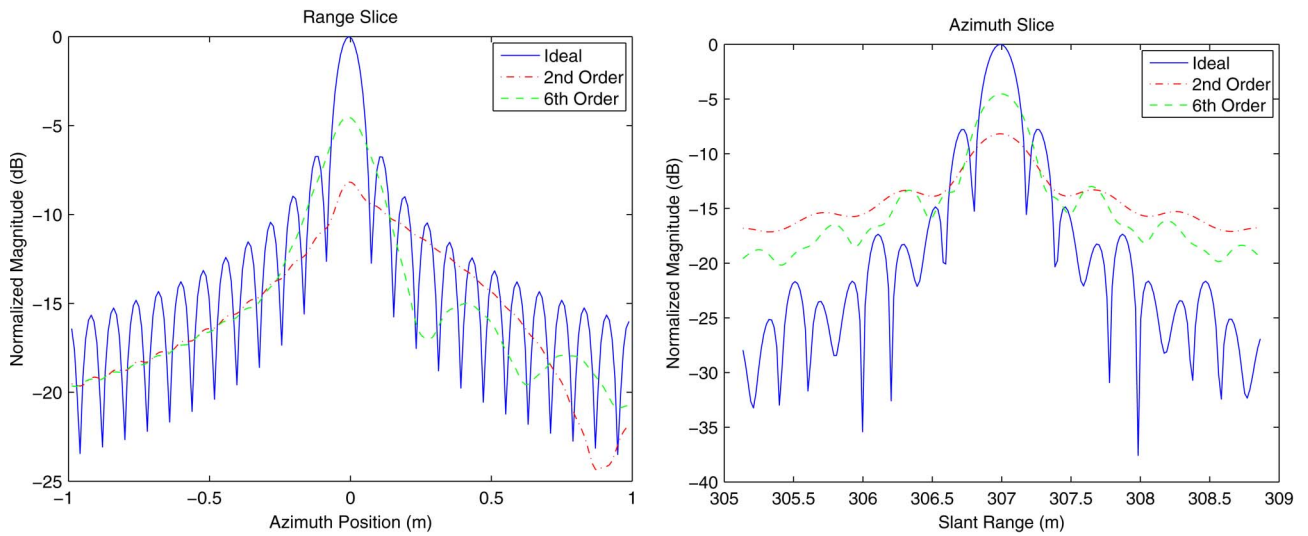

Fig. 8. For a single point target, the conjugate of (33) or (37) can be directly used to generate a focused image. Using this method, the effects of different order approximations of (37) can be seen in the image slices shown here. The cuts correspond to the data from Fig. 6(a), (b), and (d).

errors occur when neglecting the continuous-platform-motion term, or the RVP term (see Fig. 7). The effect of these larger phase errors on target focusing can be seen in Fig. 8, where a single point target is focused using the conjugate of (33) or (37). It can be seen that, as expected, target focusing is best when no approximations are used. The use of approximations in SAR algorithms introduces errors that can significantly reduce image quality. However, when higher order approximations that are closer to the ideal are used, the resulting image is better focused.

The phase of the signal from (33) with the continuous-motion term removed, expanded with n-order terms, is expressed as

$$\Phi_{S_a} = \frac{4\pi R_0 D(f_\eta)}{\lambda} + \frac{4\pi R_0 k_r t}{D(f_\eta)c_0} + \frac{\pi t^2}{K_m} + \sum_{i=3}^{n} \frac{4\pi R_0}{\lambda} Y_i \frac{t^i}{i!} \quad (37)$$

where

$$K_m = \frac{D^3(f_\eta)c_0^2}{2R_0 \lambda k_r^2 \left(D^2(f_\eta) - 1\right)} \quad (38)$$

is a useful substitution for simplifying the math.

C. Development of the Generalized FSA

The RDA and the FSA are based on the previously developed Taylor expansion. The RDA uses a second-order expansion. In the algorithm, the zeroth-order term [the first term of (37)] is the azimuth (Doppler) modulation matched during azimuth compression, range cell migration shows up in the first-order term [the second term of (37)] and is corrected by way of an interpolation, whereas the second-order term [the third term of (37)] is compensated in the secondary range compression (SRC).

TABLE I
nth-Order GFSA Processing Flow

Action	Parameter Value
1. Digitize SAR Signal $\to s_{dc0}$	$s_{dc0}(t,\eta) = \exp\left[j\left(2\pi k_r t\tau + 2\pi f_0\tau - \pi k_r \tau^2 \right) \right]$
2. 2D FFT $\to S_1$	
3. RVP Removal: $S_1 \exp\left[j\Phi_{RVP} \right]$	$\Phi_{RVP} = \frac{\pi f_r^2}{k_r}$
4. Range IFFT $\to s_2$	
5. Motion Compensation and Pre-Filter: $s_2 \exp\left[j\left(\Phi_{mc} + \Phi_{pre} \right) \right]$	$\Phi_{mc} = -2\pi t f_\eta$ $\Phi_{pre} = \sum_{i=3}^{n} \pi X_i t^i$
6. Range FFT $\to S_3$	
7. Scaling Filter: $S_3 \exp\left[j\Phi_{scale} \right]$	$\Phi_{scale} = \sum_{i=2}^{n} \pi q_i \left(f_{ref} - f_r \right)^i$
8. Range IFFT $\to s_4$	
9. Matched Filter: $s_4 \exp\left[j\Phi_{mf} \right]$	$\Phi_{mf} = \frac{4\pi t R_f k_r}{c_0} - 2\pi t f_{ref} - \frac{\pi t^2 D(f_\eta)}{K_f}$ $- \sum_{i=3}^{n} \frac{4\pi\left(\frac{i!}{4} q_i \lambda + R_f Y_i K_f^i + \frac{i!}{4} X_i K_f^i \lambda \right) t^i D^i(f_\eta)}{i! \lambda K_f^i}$
10. Range FFT $\to S_5$	
11. Azimuth Filter: $S_5 \exp\left[j\Phi_{az} \right]$	$\Phi_{az} = -\frac{4\pi R_0 D(f_\eta)}{\lambda} + \frac{4\pi f_r R_0}{c_0} - \frac{8\pi R_0^2 k_r}{c_0^2} - C_0$
12. Azimuth IFFT $\to s_6$	

$$q_2 = \frac{K_f\left(D(f_\eta) - 1 \right)}{D(f_\eta)} \ , \quad q_3 = \frac{-\left(D(f_\eta) - 1 \right) K_s K_f^2}{3 D(f_\eta)}, \quad X_3 = \frac{-\left(D(f_\eta) K_s \lambda + 2 R_f Y_3 D(f_\eta) K_f - 2 K_s \lambda - 2 R_f Y_3 K_f \right)}{3 K_f \lambda \left(D(f_\eta) - 1 \right)}$$

$$q_4 = \frac{-\left(c_0 D(f_\eta)^2 Y_3 - c_0 D(f_\eta) Y_3 + 9 X_3 D(f_\eta) K_s K_f k_r \lambda + 6 R_f Y_3 D(f_\eta) K_s K_f k_r - 9 X_3 K_s K_f k_r \lambda - 2 K_s^2 k_r \lambda - 6 R_f Y_3 K_s K_f k_r \right) K_f^3}{12 k_r \lambda D(f_\eta)}$$

$$X_4 = \frac{9 X_3 K_s K_f k_r \lambda\left(D(f_\eta) - 2 \right) + Y_3\left(D(f_\eta) - 2 \right)\left(c_0 D(f_\eta) + 6 R_f K_s K_f k_r \right) - 2 K_f k_r R_f Y_4\left(D(f_\eta) - 1 \right) - 2 K_s^2 k_r \lambda}{12 K_f k_r \lambda \left(D(f_\eta) - 1 \right)}$$

$$q_5 = \frac{\left(36 X_3 K_s^2 K_f k_r \lambda + 48 k_r X_4 K_s K_f \lambda\left(D(f_\eta) - 1 \right) + 6 Y_3 K_s\left(4 R_f K_s K_f k_r + c_0 D(f_\eta) \right) + Y_4\left(D(f_\eta) - 1 \right)\left(c_0 D(f_\eta) + 8 R_f K_s K_f k_r \right) \right) K_f^4}{60 k_r \lambda D(f_\eta)}$$

$$X_5 = \frac{36 X3 K_s^2 K_f k_r \lambda + 48 k_r X4 K_s K_f \lambda\left(D(f_\eta) - 2 \right) - 2 Y_5 k_r R_f K_f\left(D(f_\eta) - 1 \right) + 6 Y_3 K_s\left(4 R_f K_s K_f k_r + c_0 D(f_\eta) \right)}{60 K_f k_r \lambda\left(D(f_\eta) - 1 \right)}$$
$$+ \frac{Y_4\left(D(f_\eta) - 2 \right)\left(c_0 D(f_\eta) + 8 R_f K_s K_f k_r \right)}{60 K_f k_r \lambda\left(D(f_\eta) - 1 \right)}$$

For low frequencies, high bandwidths, large beamwidths, and large squints, the second-order expansion is inadequate for describing the SAR signal. This results in phase errors in the processing that cause defocusing in the final image. This paper develops a generalized FSA algorithm that addresses these errors. There are other frequency-domain algorithms that have differing methods of addresssing approximation errors, and for certain imaging scenarios, these algorithms may prove to be more accurate than the proposed method.

The FSA, as described in [11], [14], and [21], uses a third-order expansion but only compensates for the second- and third-order terms (which correspond to the SRC) at a single reference range. Recognizing the increased importance of the higher order terms for squinted data, the nonlinear FSA from [22], introduces a number of steps that can reduce the range dependence of the second- and third-order terms, providing better performance for SAR scenarios (such as squint mode) that push beyond the validity of the traditional approximations. The higher order methods lack the ability to compensate for continuous motion and are limited to, at most, the third-order term. The existing algorithms fall short with SAR parameters that cause terms higher than $n = 3$ to play a significant role. By generalizing on these approaches, the GFSA can account for terms of any order that may be needed to properly model the SAR data.

A generalized FSA that accounts for an arbitrary number of terms is beneficial for processing SAR data with a wide variety of system parameters. For a given set of SAR parameters, an appropriate number of terms can be used to maximize efficiency, accuracy, and precision in processing. Such an algorithm is now derived. The algorithm flow is shown in Table I.

The basic idea is to apply corrections for the RVP and continuous motion, apply an n-order prefilter and an n-order scaling filter that work together to reduce the range dependence of the higher order terms, and remove them for a reference range. The resulting signal is then match filtered and azimuth compressed to form a focused SAR image.

The first step is to apply a prefilter, with phase

$$H_{pre} = \sum_{i=3}^{n} \pi X_i t^i \qquad (39)$$

where X_i is solved for at a later point in this derivation and is carefully chosen to reduce the range dependence of the higher order terms and to compensate for the higher order terms at a reference range, i.e., R_f.

A range Fourier transform of the signal is now computed using the principle of stationary phase. To find the stationary point, the terms of order higher than two are neglected (the rapidly varying high-order terms do little to change the stationary point), and the derivative of $\Phi_{S_a} + H_{pre} - 2\pi f_r t$ is set to zero and solved for t, i.e.,

$$t = \frac{-\left(2R_0 k_r - f_r D(f_\eta) c_0\right) K_m}{D(f_\eta) c_0} = -(f_t - f_r) K_m \quad (40)$$

where f_t is the frequency trajectory of a target at range R_0 and is a useful substitution for working through the math, i.e.,

$$f_t = \frac{2R_0 k_r}{c_0 D(f_\eta)}. \qquad (41)$$

The phase of the signal after the range Fourier transform is

$$\Phi_{S_3} = \frac{4\pi R_0 D(f_\eta)}{\lambda} - \frac{4\pi R_0 k_r (f_t - f_r) K_m}{D(f_\eta) c_0}$$

$$+ \pi (f_t - f_r)^2 K_m + 2\pi f_r (f_t - f_r) K_m$$

$$+ \sum_{i=3}^{n} (-1)^i \left(\frac{4\pi R_0 Y_i}{\lambda i!} + \pi X_i\right)(f_t - f_r)^i K_m^i. \quad (42)$$

Combining the second term and the fourth term of (42) and again using the substitution of (41), we have

$$- \frac{4\pi R_0 k_r (f_t - f_r) K_m}{D(f_\eta) c_0} + 2\pi f_r (f_t - f_r) K_m$$

$$= \frac{2\pi (f_t - f_r) K_m (-2R_0 k_r + f_r D(f_\eta) c_0)}{D(f_\eta) c_0}$$

$$= -2\pi (f_t - f_r)^2 K_m \qquad (43)$$

which is combined with the third term of (42) and simplifies to

$$\Phi_{S_3} = \frac{4\pi R_0 D(f_\eta)}{\lambda} - \pi (f_t - f_r)^2 K_m$$

$$+ \sum_{i=3}^{n} (-1)^i \left(\frac{4\pi R_0 Y_i}{\lambda i!} + \pi X_i\right)(f_t - f_r)^i K_m^i. \quad (44)$$

A scaling filter consisting of terms of orders from two to n is now applied to the signal. The coefficients of this scaling term are derived through a series of substitutions and algebraic manipulation. They are chosen along with the prefilter terms to cancel out the range dependence of the higher order terms of the expansion of the SAR signal. The scaling filter is

$$H_{scale} = \sum_{i=2}^{n} \pi q_i (f_{ref} - f_r)^i. \qquad (45)$$

The SAR signal $(\Phi_{S_3} H_{scale})$ is expanded and algebraically rearranged with the help of the following substitutions:

$$f_t = f_{ref} + \Delta f \qquad (46)$$
$$f_{ref} = f_s - D(f_\eta) \Delta f. \qquad (47)$$

where

$$\Delta f = \frac{2(R_0 - R_f) k_r}{c_0 D(f_\eta)} \qquad (48)$$

and f_s is the scaled target frequency trajectory for a target at range R_0 that has the same shape as the reference frequency trajectory.

The signal is rearranged to match the form

$$\Phi_{S_{3b}} = \sum_{i=0}^{n} C_i (f_s - f_r)^i \qquad (49)$$

where

$$C_i = c_{hi} + \sum_{k=i}^{n} \frac{k!}{i!(k-i)!} \cdot (-K_m)^k \left(\Delta f \left(1 - D(f_\eta)\right)\right)^{(k-i)}$$

$$\cdot \left(\frac{4\pi R_0 Y_k}{k! \lambda} + \pi X_k\right)$$

$$+ \sum_{k=i}^{n} \frac{k!}{i!(k-i)!} \pi q_k \left(-\Delta f D(f_\eta)\right)^{(k-i)} \qquad (50)$$

$$c_{h0} = -\pi K_m \Delta f^2 \left(D(f_\eta) - 1\right)^2$$

$$c_{h1} = 2\pi K_m \Delta f \left(D(f_\eta) - 1\right)$$

$$c_{h2} = -\pi K_m$$

$$c_{hi} = 0 \quad \text{for } i > 2 \qquad (51)$$

where $X_i = 0$ and $Y_i = 0$ for $i < 3$, and $q_i = 0$ for $i < 2$.

The range dependence of each C_i term can be reduced by appropriately choosing the X_i's and the q_i's. Determining these values is aided by expanding each C_i about a reference range R_f. In (50), each R_0 is expanded and expressed in terms of Δf from (48):

$$R_0 = R_f + R_0 - R_f = R_f + \frac{\Delta f D(f_\eta) c_0}{2 k_r}. \qquad (52)$$

We express K_m from (38) in terms of Δf, i.e.,

$$K_m = \frac{-K_f}{K_s K_f \Delta f - 1} \qquad (53)$$

where

$$K_f = \frac{D^3(f_\eta) c_0^2}{2R_f \lambda k_r^2 \left(D^2(f_\eta) - 1\right)} \qquad (54)$$

$$K_s = \frac{\left(D^2(f_\eta) - 1\right) k_r \lambda}{c_0 D^2(f_\eta)}. \qquad (55)$$

We Taylor-expand K_m in terms of Δf, retaining up to the second order, i.e.,

$$K_m \approx K_f + K_s K_f^2 \Delta f + K_s^2 K_f^3 \Delta f^2. \qquad (56)$$

Each C_i, for $i > 0$, is rearranged to be expressed as a power series of Δf, for example

$$C_1 = \left[2\pi K_f \left(D(f_\eta) - 1\right) - 2\pi q_2 D(f_\eta)\right] \Delta f$$

$$+ \Delta f^2 \left[\frac{-2\pi R_f Y_3 K_f^3 \left(D(f_\eta) - 1\right)^2}{\lambda} + 3\pi q_3 D^2(f_\eta)\right.$$

$$- 3\pi X_3 K_f^3 \left(D(f_\eta) - 1\right)^2$$

$$\left. + - 2\pi K_s K_f^2 \left(D(f_\eta) - 1\right)\right].$$

When the coefficients of Δf are equal to zero, the range variations are eliminated. We approach this by setting the linear and quadratic terms of Δf equal to zero, resulting in $2n - 3$ equations and $2n - 3$ unknowns, for example

$$2\pi K_f \left(D(f_\eta) - 1\right) - 2\pi q_2 D(f_\eta) = 0$$

$$\frac{-2\pi R_f Y_3 K_f^3 \left(D(f_\eta) - 1\right)^2}{\lambda} + 3\pi q_3 D^2(f_\eta)$$

$$- 3\pi X_3 K_f^3 \left(D(f_\eta) - 1\right)^2 + 2\pi K_s K_f^2 \left(D(f_\eta) - 1\right) = 0$$

$$\frac{2\pi R_f Y_3 K_f^3 \left(D(f_\eta) - 1\right)}{\lambda} - 3\pi q_3 D(f_\eta)$$

$$+ 3\pi X_3 K_f^3 \left(D(f_\eta) - 1\right) - \pi K_s K_f^2 = 0. \tag{57}$$

We solve for q_i and X_i in Table I.

The linear and quadratic terms of Δf in each C_i for $i > 0$ become zero, whereas the higher order terms are small and can be neglected (an approximation that results in some small error). What remains of the SAR signal phase can be expressed as

$$\Phi_{S_{3c}} = \frac{4\pi R_0 D(f_\eta)}{\lambda} - \frac{\pi K_f}{D(f_\eta)}(f_s - f_r)^2 + C_0$$

$$+ \sum_{i=3}^{n} \pi \left[q_i + (-K_m)^i X_i + \frac{4 R_f Y_i (-K_m)^i}{i!\lambda}\right] (f_s - f_r)^i. \tag{58}$$

An inverse Fourier transform of the signal is taken, which can be approximated using the principle of stationary phase with the stationary point found using the first two terms of (58), i.e.,

$$\frac{d}{df_r}\left[\frac{4\pi R_0 D(f_\eta)}{\lambda} - \frac{\pi K_f (f_s - f_r)^2}{D(f_\eta)} + 2\pi f_r t\right] = 0$$

$$f_r = \frac{K_f f_s + t D(f_\eta)}{K_f}. \tag{59}$$

The signal phase after the inverse Fourier transform can be expressed as

$$\Phi_{s_4} = \frac{4\pi R_0 D(f_\eta)}{\lambda} + \frac{\pi t^2 D(f_\eta)}{K_f} + 2\pi t f_s + C_0$$

$$+ \sum_{i=3}^{n} \frac{4\pi \left(\frac{i!}{4} q_i \lambda + R_f Y_i K_f^i + \frac{i!}{4} X_i K_f^i \lambda\right) t^i D^i(f_\eta)}{i!\lambda K_f^i}. \tag{60}$$

A phase filter, i.e., H_{mf}, is now applied, where

$$H_{mf} = \frac{4\pi t R_f k_r}{c_0} - 2\pi t f_{ref} - \frac{\pi t^2 D(f_\eta)}{K_f}$$

$$- \sum_{i=3}^{n} \frac{4\pi \left(\frac{i!}{4} q_i \lambda + R_f Y_i K_f^i + \frac{i!}{4} X_i K_f^i \lambda\right) t^i D^i(f_\eta)}{i!\lambda K_f^i}. \tag{61}$$

The resulting signal phase is

$$\Phi_{s_{4b}} = \frac{4\pi R_0 D(f_\eta)}{\lambda} + \frac{4\pi t R_0 k_r}{c_0} + C_0. \tag{62}$$

A range Fourier transform compresses the signal in range, i.e.,

$$\int_{\frac{2R_0}{c_0}}^{\frac{2R_0}{c_0} + T_p} s_{4b} \exp\left[-j\left(2\pi t f_r\right)\right] dt$$

$$= \frac{-jc_0}{2\pi \left(2R_0 k_r - f_r c_0\right)}$$

$$\cdot e^{\left[j\left(\frac{4\pi R_0 D(f_\eta)}{\lambda} - \frac{4\pi f_r R_0}{c_0} + \frac{8\pi R_0^2 k_r}{c_0^2} + C_0 - 2\pi f_r T_p\right)\right]}$$

$$\cdot \left[\exp\left[j 2\pi f_r T_p\right] - \exp\left[j\frac{4\pi R_0 k_r T_p}{c_0}\right]\right]$$

$$= T_p \cdot \text{sinc}\left(\frac{\pi T_p \left(f_r c_0 - 2R_0 k_r\right)}{c_0}\right)$$

$$\cdot e^{\left[j\left(\frac{4\pi R_0 D(f_\eta)}{\lambda} - \frac{4\pi f_r R_0}{c_0} + \frac{8\pi R_0^2 k_r}{c_0^2} + C_0 - \pi f_r T_p + \frac{2\pi R_0 k_r T_p}{c_0}\right)\right]}. \tag{63}$$

The last two terms in the exponential on the last line of (63) are zero at the peak of the sinc function and can be ignored.

The final azimuth matched filter is now applied, i.e.,

$$H_{az} = -\frac{4\pi R_0 D(f_\eta)}{\lambda} + \frac{4\pi f_r R_0}{c_0} - \frac{8\pi R_0^2 k_r}{c_0^2} - C_0 \tag{64}$$

and an inverse Fourier transform results in the focused image.

Examples of the results of the new algorithm are illustrated with a SAR simulation of a point target. In the simulation, the platform moves in a straight line at 50 m/s, flying past a nearby point target. Without squint, the antenna is pointed perpendicular to the flight path. The simulation results are as follows: Fig. 9 shows a comparison of a no-squint simulation processed with the traditional FSA in [11] and with the proposed generalized algorithm (the GFSA) with only a second-order approximation. Fig. 10 shows a point target with a $15°$ squint and the same SAR parameters as Fig. 9 and processed with the traditional FSA and the GFSA with orders $n = 2$ and $n = 3$. The squint makes it so that the SAR data can no longer be accurately modeled using the approximations in the FSA. The GFSA with $n = 2$ performs better with the price of a little extra processing burden (20% more processing time). Including the third-order term further improves the performance while approximately doubling the processing time.
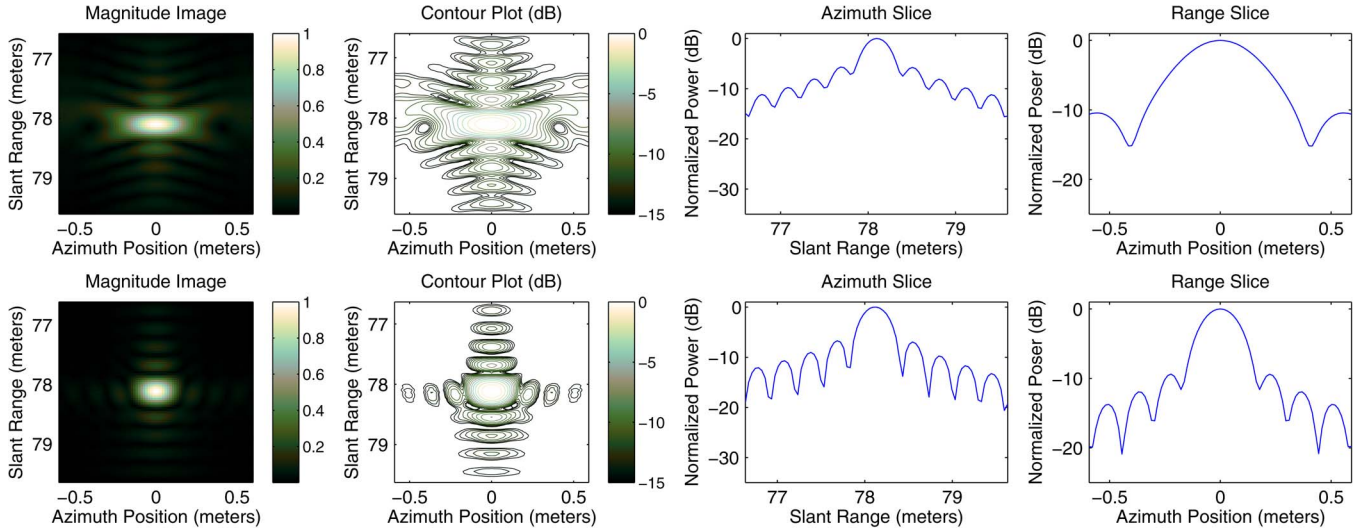
Fig. 9. Simulated SAR data for a point target with a bandwidth from 2.5 to 3 GHz and a 20° beamwidth with no squint. The top row shows the results of processing the data with the FSA, with the target at the reference range for the SRC. The bottom row shows the results of processing the data with the proposed generalized FSA with $n = 2$. The description of the columns is the same as in Fig. 4.
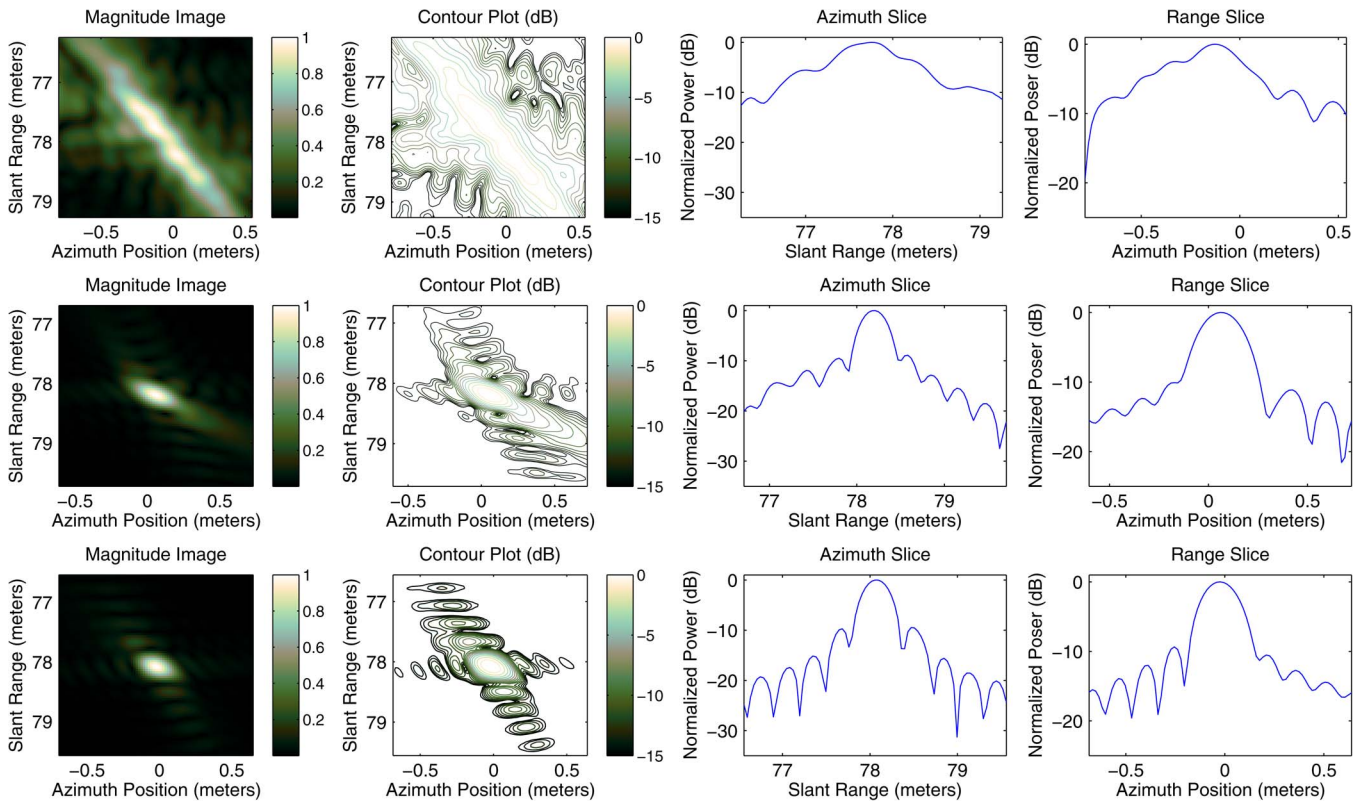

Fig. 10. Simulated SAR data for a point target with a bandwidth from 2.5 to 3 GHz and a 20° beamwidth with a 15° squint. The data are processed with the FSA in the top row, the GFSA with $n = 2$ in the middle row, and the GFSA with $n = 3$ in the bottom row. The description of the columns is the same as in Fig. 4.

If we simulate SAR data at an even larger squint angle ($> 40°$), the traditional FSA does not work. In Fig. 11, we observe the focus improving as additional terms from the Taylor expansion are included in the processing.

For a user of the GFSA, the order can be increased to meet image quality specifications for more demanding SAR parameters. The limit of utility is reached when the processing time holds no advantage over backprojection, or the numerical

accuracy of the computer for calculating high-order terms introduces error [26].

V. CONCLUSION

While the continuous motion of the radar platform creates some unwelcome issues for processing LFM-CW SAR data, the problems can be dealt with, allowing for precision processing
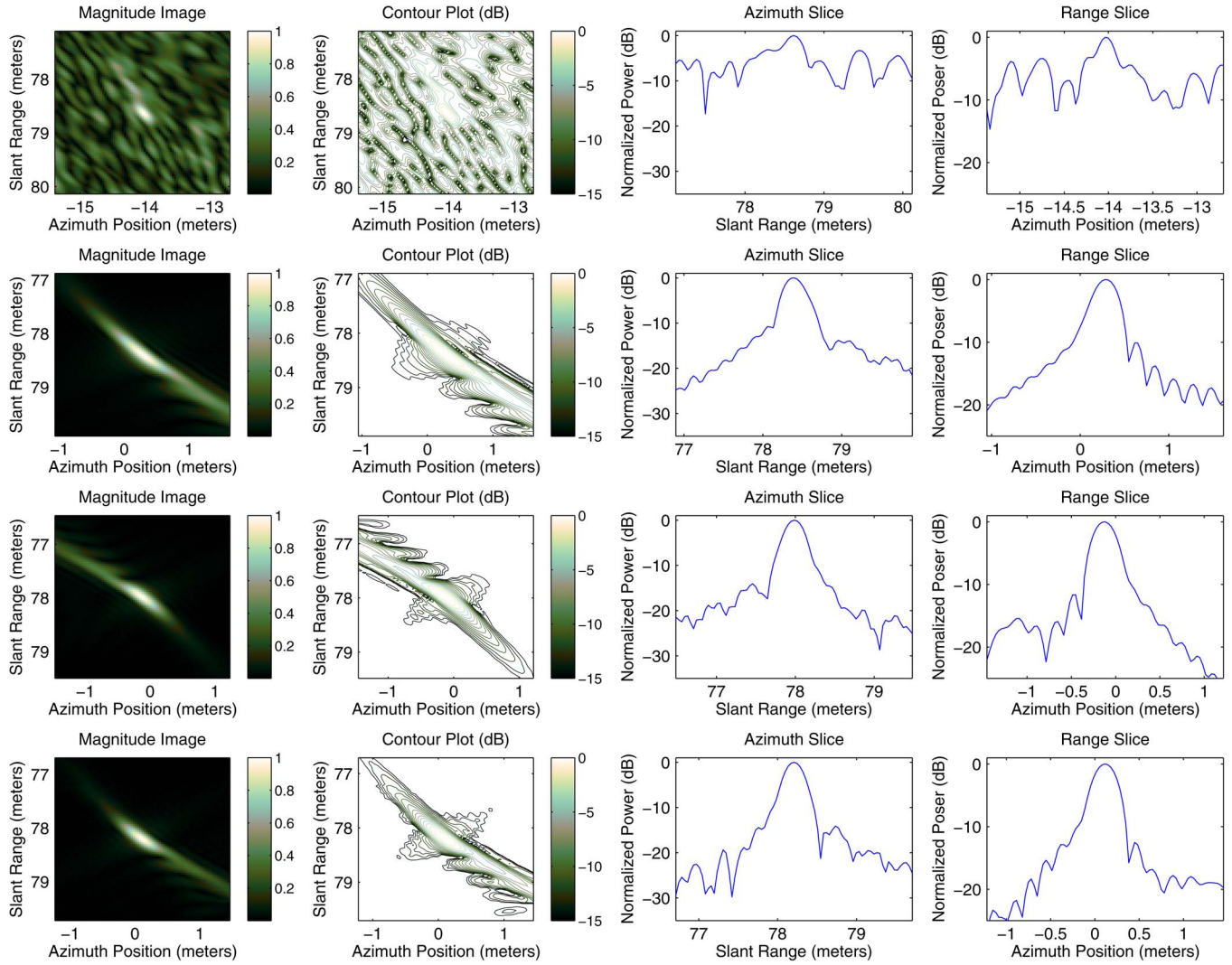
Fig. 11. Simulated SAR data for a point target with a bandwidth from 2.5 to 3 GHz and a $20°$ beamwidth with a $43°$ squint. The top row shows the data processed using the FSA. The second row shows the results of the generalized FSA with $n = 2$. The third and fourth rows show the results with $n = 3$ and $n = 4$, respectively. The FSA completely breaks down while the algorithm proposed in this paper shows results improving with each additional order included in the processing. The description of the columns is the same as in Fig. 4.

in a variety of applications. The failings of approximations made in deriving traditional SAR processing algorithms can be overcome by taking a general approach to the LFM-CW SAR signal. This paper has demonstrated a robust continuous motion correction for arbitrary flight paths, both precise and approximate LFM-CW SAR backprojection algorithms, and a generalized FSA allowing for an arbitrary number of terms from a Taylor series expansion. These algorithms extend the utility of LFM-CW SAR systems, allowing operation with a wider variety of system parameters and in nearly any imaging scenario.

APPENDIX A
CALCULATION OF THE TWO-WAY TIME-OF-TRAVEL TO A TARGET

Using the slant range geometry shown in Fig. 12, we assign X_1 to the location of the radar at time $\eta + t$ and X_2 to the location at $\eta + t - \tau$, where η is slow time. The calculation of τ is complicated by the motion of the aircraft but can be approximated.
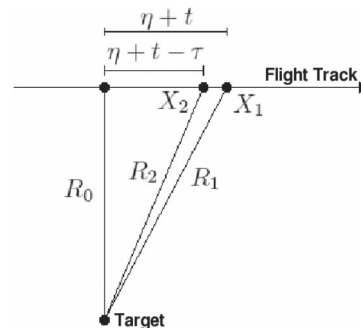

Fig. 12. SAR imaging geometry, the platform flies in a line following the arrow. The radar echo received at point X_1 was transmitted toward the target at point X_2. The total time-of-flight for the signal can be calculated using (69).

In order to precisely determine τ, we define a point x_h approximately halfway between X_1 and X_2, i.e.,

$$X_h = X_2 + \frac{R_2}{c_0}v = X_1 - \frac{R_1}{c_0}v \qquad (65)$$

where R_1 and R_2 are the distances to the target from points X_1 and X_2, respectively, defined as

$$R_1 = \sqrt{R_0^2 + X_1^2} \tag{66}$$

$$R_2 = \sqrt{R_0^2 + X_2^2}. \tag{67}$$

We also know that $X_1 = (\eta + t)v$, from which we know R_1. That leaves us with unknowns X_2 and R_2, which we solve for

$$X_2 = \frac{-v^3 R_1}{c_0 (c_0^2 - v^2)} + \frac{v^2 X_1}{c_0^2 - v^2} + X_1 - \frac{R_1 v}{c_0}$$
$$- \frac{v \sqrt{-v^2 R_0^2 c_0^2 + c_0^4 R_0^2 - 2c_0^3 X_1 R_1 v + c_0^2 R_1^2 v^2 + c_0^4 X_1^2}}{c_0 (c_0^2 - v^2)}. \tag{68}$$

We now have all the pieces to calculate τ, i.e.,

$$\tau = \frac{R_1 + R_2}{c_0} \tag{69}$$

which can be used in (1) or (4).

A very close approximation is to assume that the ranges R_1 and R_2 are the same (for spaceborne SAR, they can differ by as much as several meters, but for airborne applications, they only differ by, at most, a few millimeters, and much less than that for low-altitude operation); thus, the expression for τ can be simplified to $\tau = 2R(t, \eta)/c_0$, where $R(t, \eta) = \sqrt{R_0^2 + v^2(t + \eta)^2}$, and R_0 is the range of closest approach to the target.

REFERENCES

[1] A. Meta, J. J. M. de Wit, and P. Hoogeboom, "Development of a high resolution airborne millimeter wave FM-CW SAR," in *Proc. 1st EURAD*, Amsterdam, The Netherlands, Oct. 2004, pp. 209–212.

[2] M. Edrich, "Design overview and flight test results of the miniaturised SAR sensor MISAR," in *Proc. 1st EURAD*, Amsterdam, The Netherlands, Oct. 2004, pp. 205–208.

[3] M. Edrich, "Ultra-lightweight synthetic aperture radar based on a 35 GHz FMCW sensor concept and online raw data transmission," *IEE Proc. Radar, Sonar Navigat.*, vol. 153, no. 2, pp. 129–134, Apr. 13, 2006.

[4] A. Meta, P. Hakkaart, F. V. D. Zwan, P. Hoogeboom, and L. P. Ligthart, "First demonstration of an X-band airborne FMCW SAR," in *Proc. 6th Eur. Conf. Synthetic Aperture Radar*, Dresden, Germany, May 2006.

[5] E. C. Zaugg, D. L. Hudson, and D. G. Long, "The BYU μSAR: A Small, Student-Built SAR for UAV Operation," in *Proc. Int. Geosci. Remote Sens. Symp.*, Denver, CO, USA, Aug. 2006, pp. 411–414.

[6] J. F. Nouvel, S. Roques, and O. R. du Plessis, "A low-cost imaging radar: DRIVE on board ONERA motorglider," in *Proc. Int. Geosci. Remote Sens. Symp.*, Barcelona, Spain, Jul. 23–28, 2007, pp. 5306–5309.

[7] P. Almorox-González et al., "Portable high resolution LFM-CW radar sensor in millimeter-wave band," in *Proc. SENSORCOMM*, Valencia, Spain, pp. 5–9, Oct. 2007.

[8] J. T. González-Partida, P. Almorox-González, M. Burgos-Garcia, and B. P. Dorta-Naranjo, "SAR system for UAV operation with motion error compensation beyond the resolution cell," in *Sensors*, vol. 8, no. 5, pp. 3384–3405, 2008.

[9] M. Edwards, D. Madsen, C. Stringham, A. Margulis, B. Wilson, and D. G. Long, "MicroASAR: A small, robust LFM-CW SAR for operation on UAVs and small aircraft," in *Proc. Int. Geosci. Remote Sens. Symp.*, Boston, MA, USA, Jul. 6–11, 2008, pp. V-514–V-517.

[10] J. J. M. de Wit, A. Meta, and P. Hoogeboom, "Modified range-Doppler processing for FM-CW synthetic aperture radar," *IEEE Geosci. Remote Sens. Lett.*, vol. 3, no. 1, pp. 83–87, Jan. 2006.

[11] A. Meta, P. Hoogeboom, and L. P. Ligthart, "Non-linear frequency scaling algorithm for FMCW SAR data," *Proc. 3rd Eur. Radar Conf.*, Sep. 2006, pp. 9–12.

[12] A. Meta, P. Hoogeboom, and L. P. Ligthart, "Signal processing for FMCW SAR," in *IEEE Trans. Geosci. Remote Sens.*, vol. 45, no. 11, pp. 3519–3532, Nov. 2007.

[13] E. C. Zaugg and D. G. Long. "Theory and application of motion compensation for LFM-CW SAR," *IEEE Trans. Geosci. Remote Sens.*, vol. 46, no. 10, pp. 2990–2998, Oct. 2008.

[14] Z. H. Jiang and K. Huang-Fu, "Squint LFMCW SAR data processing using Doppler-centroid-dependent frequency scaling algorithm," *IEEE Trans. Geosci. Remote Sens.*, vol. 46, no. 11, pp. 3535–3543, Nov. 2008.

[15] Wen-Qin Wang, Qicong Peng, and Jingye Cai, "Waveform-diversity-based millimeter-wave UAV SAR remote sensing," *IEEE Trans. Geosci. Remote Sens.*, vol. 47, no. 3, pp. 691–700, Mar. 2009.

[16] L. Yunhua, S. Hongjun, G. Yang, D. Yunkai, and R. Wang, "Modified frequency scaling processing for FMCW SAR," in *Proc. Int. Geosci. Remote Sens. Symp.*, pp. 2129–2132, Jul. 22–27, 2012.

[17] R. Wang et al., "Focus FMCW SAR data using the wavenumber domain algorithm," *IEEE Trans. Geosci. Remote Sens.*, vol. 48, no. 4, pp. 2109–2118, Apr. 2010.

[18] A. Ribalta, "Time-domain reconstruction algorithms for FMCW-SAR," in *IEEE Geosci. Remote Sens. Lett.*, vol. 8, no. 3, pp. 396–400, May 2011.

[19] A. Ribalta, "High resolution SAR image reconstruction: The generalized backprojection algorithm," in *Proc. Int. Geosci. Remote Sens. Symp.*, pp. 363–365, Jul. 24–29, 2011.

[20] W. G. Carrara, R. S. Goodman, and R. M. Majewski, *Spotlight Synthetic Aperture Radar: Signal Processing Algorithms*. Norwood, MA, USA: Artech House, 1995.

[21] J. Mittermayer, A. Moreira, and O. Loffeld, "Spotlight SAR data processing using the frequency scaling algorithm," *IEEE Trans. Geosci. Remote Sens.*, vol. 37, no. 5, pp. 2198–2214, Sep. 1999.

[22] L. Jin and X. Liu, "Nonlinear frequency scaling algorithm for squint spotlight SAR data processing," in *EURASIP J. Adv. Signal Process.*, vol. 2008, 2008, Art. ID. 657081.

[23] O. Frey, C. Magnard, M. Ruegg, E. Meier, "Focusing of airborne synthetic aperture radar data from highly nonlinear flight tracks," in *IEEE Trans. Geosci. Remote Sens.*, vol. 47, no. 6, pp. 1844–1858, Jun. 2009.

[24] "CUDA Zone—The Resource for CUDA Developers." Aug. 3, 2009 [Sep. 22, 2009]. [Online]. Available: http://www.nvidia.com/object/cuda_home.html#state=detailsOpen;aid=057f342d-84b4-4a12-ae35-5208c51ed958

[25] M. C. Edwards, E. C. Zaugg, D. G. Long, R. Christiansen, and A. Margulis, "A small, manned aircraft as a testbed for radar sensor development," in *Proc. SPIE Defense, Security+Sensing*, Apr. 2009, vol. 7308, Art. ID. 730807.

[26] E. C. Zaugg and D. G. Long, "Generalized frequency-domain SAR processing," *IEEE Trans. Geosci. Remote Sens.*, vol. 47, no. 11, pp. 3761–3773, Nov. 2009.

Evan C. Zaugg (S'06–M'11) received the Ph.D. degree in electrical engineering from Brigham Young University (BYU), Provo, UT, USA, in 2010.

As a Ph.D. student, he performed theoretical work in generalization of the signal processing for pulsed and continuous-wave synthetic aperture radar (SAR) and did design, testing, and assembly of the BYU SAR systems. At ARTEMIS, Inc., he continues his research and development of SAR systems, data processing, and exploitation, including advanced SAR image formation algorithms, ground moving target indicators, interferometry, and change detection. He has more than 15 publications on innovative SAR theory, systems, and processing.

David G. Long (S'80–SM'98–F'08) received the Ph.D. degree in electrical engineering from the University of Southern California, Los Angeles, CA, USA, in 1989.

From 1983 to 1990, he worked for NASA's Jet Propulsion Laboratory (JPL), where he developed advanced radar remote sensing systems. While at JPL, he was the Project Engineer on the NASA Scatterometer project, which flew from 1996 to 1997. He also managed the Scanning Scatterometer project, the precursor to SeaWinds that was launched in 1999 on QuikSCAT and 2002 on ADEOS-II. He is currently a Professor with the Department of Electrical and Computer Engineering, Brigham Young University, Provo, UT, USA, where he teaches upper division and graduate courses in communications, microwave remote sensing, radar, and signal processing and is the Director of the Brigham Young University Center for Remote Sensing. He is the Principal Investigator on several NASA-sponsored research projects in remote sensing. He has over 400 publications in various areas, including signal processing, radar scatterometry, and synthetic aperture radar. His research interests include microwave remote sensing, radar theory, space-based sensing, estimation theory, signal processing, and mesoscale atmospheric dynamics.

Dr. Long has received the NASA Certificate of Recognition several times and is an Associate Editor for the IEEE GEOSCIENCE AND REMOTE SENSING LETTERS.